The Astrophysical Journal, 798:25 (10pp), 2015 January 1 doi:10.1088/0004-637X/798/1/25

GRAVITATIONAL WAVES FROM MASSIVE MAGNETARS FORMED IN BINARY NEUTRON STAR MERGERS

Simone Dall'Osso[1], Bruno Giacomazzo[2,3], Rosalba Perna[4], and Luigi Stella[5]
[1] Theoretical Astrophysics, University of Tübingen, auf der Morgenstelle 10 D-72076, Germany; simone.dallosso@uni-tuebingen.de
[2] Physics Department, University of Trento, via Sommarive 14, I-38123 Trento, Italy
[3] INFN-TIFPA, Trento Institute for Fundamental Physics and Applications, via Sommarive 14, I-38123 Trento, Italy
[4] Department of Physics and Astronomy, Stony Brook University, Stony Brook, NY 11794, USA
[5] INAF-Osservatorio Astronomico di Roma, via di Frascati 33, I-00040 Monteporzio Catone, Roma, Italy
Received 2014 July 29; accepted 2014 October 1; published 2014 December 16

ABSTRACT

Binary neutron star (NS) mergers are among the most promising sources of gravitational waves (GWs), as well as candidate progenitors for short gamma-ray bursts (SGRBs). Depending on the total initial mass of the system and the NS equation of state (EOS), the post-merger phase can be characterized by a prompt collapse to a black hole or by the formation of a supramassive NS, or even a stable NS. In the latter cases of post-merger NS (PMNS) formation, magnetic field amplification during the merger will produce a magnetar and induce a mass quadrupole moment in the newly formed NS. If the timescale for orthogonalization of the magnetic symmetry axis with the spin axis is smaller than the spindown time, the NS will radiate its spin down energy primarily via GWs. Here we study this scenario for the various outcomes of NS formation: we generalize the set of equilibrium states for a twisted torus magnetic configuration to include solutions that, for the same external dipolar field, carry a larger magnetic energy reservoir; we hence compute the magnetic ellipticity for such configurations, and the corresponding strength of the expected GW signal as a function of the relative magnitude of the dipolar and toroidal field components. The relative number of GW detections from PMNSs and from binary NSs is a very strong function of the NS EOS, being higher ($\sim$1%) for the stiffest EOSs and negligibly small for the softest ones. For intermediate-stiffness EOSs, such as the $n = 4/7$ polytrope recently used by Giacomazzo and Perna or the GM1 used by Lasky et al., the relative fraction is $\sim$0.3%; correspondingly, we estimate a GW detection rate from stable PMNSs of $\sim$0.1–1 yr^{-1} with advanced detectors, and of $\sim$100–1000 yr^{-1} with detectors of third generation such as the Einstein Telescope. Measurement of such GW signals would provide constraints on the NS EOS and, in connection with an SGRB, on the nature of the binary progenitors giving rise to these events.

Key words: equation of state – gravitational waves – magnetic fields – stars: magnetars – stars: neutron

1. INTRODUCTION

Binary neutron star (BNS) mergers are among the most powerful sources of gravitational waves (GWs) that are expected to be detected in the next few years by ground-based detectors, such as the advanced LIGO and Virgo (Abadie et al 2010). BNSs are also the focus of theoretical modeling of short gamma-ray bursts (SGRBs) since their merger can lead to the production of relativistic jets and hence generate powerful gamma-ray emissions (e.g., see Berger 2014 for a recent review). One of the main scenarios of BNS mergers predicts the formation of a spinning black hole (BH) surrounded by an accretion torus soon after the merger, i.e., in less than approximately one second (see Faber & Rasio 2012 for a recent review of BNS merger simulations).

It is, however, known that the total mass of the binary, together with the NS equation of state (EOS), can lead to different dynamics in the post-merger phase (e.g., see Baiotti et al 2008; Hotokezaka et al. 2011; Bauswein et al 2013; Andersson et al 2013). Depending on the initial mass of the system, and going from high-mass to low-mass BNSs, the end result of the merger could be a prompt collapse to BH (e.g., Rezzolla et al 2010) or the formation of a post-merger NS (PMNS). The latter could be a *hypermassive* PMNS (i.e., supported by strong differential rotation) which will collapse in less than one second (e.g., Baiotti et al 2008), a *supramassive* PMNS (i.e., supported by rapid and uniform rotation), and, if the masses are sufficiently low (e.g., $\sim$1.22 $M_\odot$ in the case of Giacomazzo & Perna 2013), even a *stable* PMNS that will not collapse to a BH independently of its rotation.

The discovery of two NSs of $\sim 2\,M_\odot$ (Demorest et al. 2010; Antoniadis et al. 2013) has opened the possibility that indeed a supramassive, or a stable NS, may be the end result in a significant number of BNS mergers. Moreover, recent observations of X-ray plateaus in SGRBs could support the possibility, that at least in some SGRBs, a supramassive or a stable NS with a strong magnetic field was formed after the merger (Rowlinson et al 2013; see also Metzger et al. 2008; Dall'Osso et al. 2011). The recent discovery of fast radio bursts (Lorimer et al. 2007; Thornton et al. 2013) has also been interpreted as the final signal of a supramassive rotating NS that collapses to a BH due to magnetic braking (Falcke & Rezzolla 2014; cf. Ravi & Lasky 2014). Recent numerical simulations of BNS mergers followed the formation of a stable PMNS with a large mass ($\lesssim$2.36 $M_\odot$), a relatively large radius ($\approx$15 km), a spin close to break up and a large degree of differential rotation (Giacomazzo & Perna 2013). Due to the combined effect of Kelvin–Helmholtz instabilities and dynamo action, a strong amplification of the internal magnetic field occurs promptly and the PMNS settles into uniform rotation, with millisecond spin and a strongly twisted interior magnetic field. The resulting picture is reminiscent of the so-called standard magnetar formation scenario (Duncan & Thompson 1992), in which an ultramagnetized NS is formed in the core-collapse of a massive star by tapping a fraction of the energy in the differential rotation of a fast-spinning proto-NS.

Such a scenario would have a very important role because, along with explaining some electromagnetic observations, the millisecond spinning, ultramagnetized PMNS could provide a long-lasting GW signal, which would be extremely valuable

for studying the EOS of NS matter (e.g., Takami et al 2014) in analogy with what was proposed for magnetars born in the core-collapse of massive stars (Duncan & Thompson 1992; Zhang & Mészáros 2001; Cutler 2002; Stella et al. 2005; Bucciantini et al. 2006, 2008; Dall'Osso & Stella 2007; Dall'Osso et al. 2009; Metzger et al. 2011).

In this work, we address the possible long-lasting GW signal following the BNS merger due to the spindown of a magnetically deformed PMNS, based on the picture studied by Cutler (2002), Stella et al. (2005), and Dall'Osso et al. (2009). In Section 2, we analyze the main steps that characterize this picture and introduce a physical model to calculate the properties of the strongly magnetized PMNS. In Section 3, we address the role of the NS EOS in determining the possible outcome of a merger and compare expectations with available data from known BNSs. In Section 4, we calculate the strength of the expected GW signals and, based on the inferred properties of the BNS population, estimate the rate at which stable or supramassive PMNSs could be detected, relative to the total population of BNS mergers, by the forthcoming generation of detectors.

2. A GENERIC SCENARIO FOR GW EMISSION

The general scenario for efficient GW emission from the newly formed, millisecond spinning and strongly magnetized PMNS can be summarized as follows (see Cutler 2002).

1. The mechanism for field amplification at the merger implies that the axis of symmetry of the strongly twisted magnetic field will start almost aligned with the spin axis.
2. The NS is distorted into an ellipsoidal shape by the anisotropic magnetic stress. Free body precession will be excited by even a small misalignement between the magnetic symmetry axis and the spin axis. We indicate the tilt angle with χ from here on.
3. Strictly speaking, the largest deformation of the PMNS shape is caused by its fast rotation at $\sim$ kHz frequency. The rotationally induced distortion is, however, always aligned with the instantaneous spin axis and thus plays no role in the dynamics of free body precession (see Cutler 2002 for a detailed discussion of this point). This is why we only consider the magnetically induced distortion.
4. The energy of freebody precession is viscously dissipated and the conserved angular momentum is redistributed in the stellar interior. As a result, the PMNS ends up rotating around an axis that corresponds to its largest moment of inertia, so as to minimize spin energy at constant angular momentum.
5. A toroidal magnetic field produces a prolate ellipsoid, i.e., one in which the smallest moment of inertia is the one relative to the axis of symmetry of the magnetic field.
6. For a prolate ellipsoid, viscous dissipation implies that the magnetic symmetry axis is driven orthogonal to the spin axis. This maximizes the time-varying quadrupole moment of the rotating top, hence its GW emission efficiency.

After this sequence of events, the PMNS becomes a potential source of GWs. The strength of the emitted signal will be determined by the strength of the GW-induced spindown torque, and by the competition with the additional torque due to magnetic dipole braking (see Section 2.3).

2.1. Growth of the Internal Field: Theoretical and Observational Support

General relativistic MHD simulations of BNS mergers show that a strong toroidal field is always produced during the merger (Giacomazzo et al. 2011), even starting with a purely poloidal magnetic field. For the specific choice of an initial dipole $\sim 10^{12}\,G$, Giacomazzo & Perna (2013) showed that hydrodynamical instabilities during the merger can generate poloidal and toroidal components of at least $\sim 10^{13}\,G$; further amplification was seen while following the remnant's evolution for tens of milliseconds after the merger, with the energy in the toroidal field becoming larger than the poloidal energy by at least one order of magnitude. It is expected that the interior field can grow even stronger in the subsequent evolution, up to $\gtrsim 10^{16}\,G$, as suggested by recent local simulations at very high resolution (Zrake & MacFadyen 2013; Giacomazzo et al. 2014).

The timing and X-ray emission properties of the galactic population of magnetars suggest the presence of internal fields much stronger than the external dipoles (e.g., Dall'Osso et al. 2012). Internal magnetic fields of $\sim 10^{15}\,G$ are also derived by energy arguments, in particular, based on the 2004 Giant Flare from SGR 1806 (Stella et al. 2005). Recent observations (Rea et al. 2010, 2012, 2013) have revealed outbursting behavior and enhanced quiescent X-ray luminosity in a few NSs with dipolar fields in the 5×10^{12} to $5 \times 10^{13}\,G$ range, well below the few $\times 10^{14}\,G$ strength believed necessary to cause crustal fractures, trigger magnetic outbursts, and enhance the NS quiescent X-ray luminosity. By means of magnetothermal simulations of the NS crust, it was shown (Perna & Pons 2011; Pons & Perna 2011; Viganò et al. 2013) that magnetic stresses can fracture the crust even in NSs with relatively low external dipoles, as long as the internal toroidal field is very strong ($\gtrsim$ a few $\times 10^{15}\,G$), thus accounting for the outbursts of "low-B" field NSs.

2.2. The Twisted-torus Magnetic Configuration

The magnetic field of the PMNS at the end of the merger phase is expected to quickly settle into an equilibrium state, driven by the growth of magnetic instabilities on very short timescales.

A general equilibrium configuration for a wide range of initial conditions was found by means of extensive numerical simulations (Braithwaite & Nordlund 2006; Braithwaite 2009) in the form of the so-called twisted-torus, i.e., a linked toroidal-poloidal magnetic field. The poloidal component contains an inner bundle of field lines that close inside the NS and therefore do not contribute to the exterior field.

We consider here such a configuration and, following the existing literature, restrict attention to the case where the toroidal field does not reach the exterior, which requires that it remains confined within the close-field-line region. While only a part of the poloidal flux extending beyond the NS surface contributes to the exterior dipolar field, both closed and open poloidal field lines contribute to the total poloidal energy. The latter will thus depend explicitly on the size of the closed field line region, and might exceed the energy of the (exterior) dipole even by a large factor.

In order to derive the relevant physical properties of a magnetized PMNS, we have slightly generalized previous treatments of the twisted torus (Mastrano et al. 2011; Mastrano & Melatos 2012) to allow for an arbitrary size of the closed-field-line region, according to the prescription of Akgün et al. (2013). Details of this generalization are provided in Appendix A1. We have then chosen a specific configuration of the magnetic field

within a class of solutions that, compared to previous studies of the twisted torus, allow for (1) a larger magnetic energy reservoir in the NS interior and (2) stabilization of a stronger toroidal field, for the same strength of the exterior dipole. While our procedure is valid, in general, the specific choice of the magnetic field geometry determines all numerical estimates. A detailed study of how these change according to the size of the closed-field-line region will appear in a separate work (in preparation).

2.2.1. Magnetic Ellipticity

The anisotropic stress due to the interior magnetic field will induce a distortion of the PMNS shape, hence a mass quadrupole moment $Q \sim I_0 \epsilon_B$ that is best expressed in terms of the moment of inertia of the unperturbed star, I_0, and its *total* magnetic ellipticity, ϵ_B. The latter can be formally defined as the fractional difference between two main eigenvalues of the moment of inertia tensor. Let the axis of symmetry of the internal field be the z axis, and the x and y axes lie in a plane perpendicular to it, then $\epsilon_B \equiv (I_{zz} - I_{xx})/I_0$. To calculate the magnetically induced ellipticity, we followed Mastrano et al. (2011), adjusting the calculations to our different choice for the interior field configuration. More details about our procedure are given in Appendix A2.

Our main result is the following numerical expression,

$$\epsilon_B \simeq 2.725 \times 10^{-6} \left(\frac{B_{dip}}{10^{14}\ G}\right)^2 \left(\frac{R_*}{15\,\mathrm{km}}\right)^4 \quad (1)$$

$$\times \left(\frac{M_*}{2.36\,M_\odot}\right)^{-2} \left(1 - 0.73\frac{E_T}{E_{pol}}\right), \quad (2)$$

where the (positive) contribution of the poloidal component and the (negative) contribution of the toroidal component are consistently accounted for.[6]

2.2.2. Interior Magnetic Field versus Exterior Dipole

Stability considerations set a maximum to the allowed toroidal-to-poloidal field ratio. Stable stratification of NS matter allows for much larger values of this ratio than previously thought (Reisenegger 2009; Akgün et al. 2013). We derived the maximum allowed ratio for the specific magnetic configuration represented in Figure 1, by following the procedure of Akgün et al. (2013). Since our discussion here is necessarily limited in scope, we refer the reader to that paper for a thorough derivation. A generalisation of our calculations to arbitrary magnetic fields is postponed to a forthcoming paper. Adopting the general expression of the NS field given in Section 1, we integrate its two components within their respective domains (see Section 2.2) and obtain the total energies

$$E_{pol} \simeq 64.675 \eta_{pol}^2 B_0^2 R_{ns}^3 = 0.0055 b_{pol}^2 B_0^2 R_{ns}^3$$

$$\simeq 5.5 \times 10^{47} \left(\frac{B_{dip}}{10^{14}\ \mathrm{G}}\right)^2 \left(\frac{R_{ns}}{15\ \mathrm{km}}\right)^3 \mathrm{erg} \quad (3)$$

$$E_T \simeq 9.152 \eta_T^2 B_0^2 R_{ns}^3 = 0.0105 b_T^2 B_0^2 R_{ns}^3 \simeq 11.6 \left(\frac{b_T}{b_{pol}}\right)^2 E_{pol}, \quad (4)$$

[6] Mastrano et al. (2011; Mastrano & Melato 2012) give ϵ_B versus $\Lambda = E_{pol}/(E_{pol} + E_T)$. The latter goes from 0 (for a purely toroidal field) to 1 (for a purely poloidal field). In terms of Λ, Equation (1) becomes $\epsilon_B \simeq 4.7 \times 10^{-6} (B_{dip}/10^{14}\mathrm{G})^2 (1 - 0.422/\Lambda)$, omitting R_* and M_*.

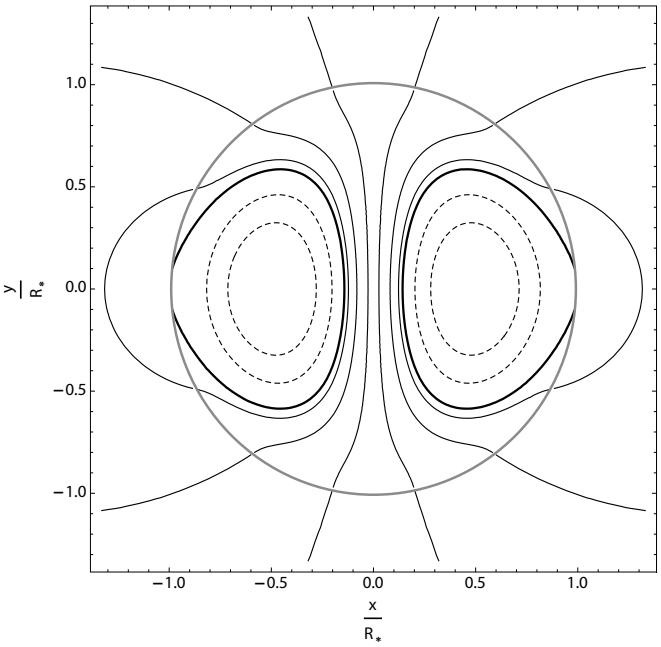

Figure 1. Representation of magnetic field lines in the chosen configuration. The NS surface is indicated by the thick gray dashed circle. A mixed toroidal–poloidal field in the NS interior is matched to a pure dipole in the exterior with no surface currents. The toroidal field is confined within the region of closed poloidal field lines, the boundary of which is indicated by the thick closed curve. The extension of this region can be adjusted freely at a fixed strength of the exterior dipole, B_{dip}. This adjustment induces: (1) a change in the total poloidal field energy, without changing B_{dip}; (2) a change in the total NS ellipticity, ϵ_B, at fixed values of B_{dip} and E_T (see Section 2.2.1); (3) a change in the stability threshold for the toroidal-to-poloidal field ratio (see Section 2.2.2).

where $\eta_{pol,T}$ are dimensionless constants measuring the relative strength of the two field components, B_0 is the field normalization, $B_{dip} = 2\eta_{pol} B_0$, and the following definitions hold: $B_{pol}^{(max)} \equiv b_{pol} B_0$, $B_T^{(max)} \equiv b_T B_0$, $B^{(max)}$, indicating the maximum value of either field component inside the NS volume.

With these expressions, and after calculating the parameters k_{hydro}, k_{pol}, and k_T defined in Equations (79)–(82) of Akgün et al. (2013), we derived the condition for stability of the magnetic field in terms of the energy ratio between its components (see Equation (83) of Akgün et al. 2013)

$$\frac{E_{pol}}{E_T} \gtrsim 0.00894 \frac{b_T^2}{(\Gamma/\gamma - 1)\, p}, \quad (5)$$

where $\Gamma = 1 + 1/n$ for a polytrope with index n, γ is the adiabatic index of the NS fluid,[7] and $p = 8\pi P_c / B_0^2$, with P_c as the NS central pressure. The ratio b_T^2/p is derived by inverting

$$\frac{E_T}{E_G} \simeq 0.1098 \frac{b_T^2}{p}, \quad (6)$$

where $E_G = (3/5 - n)(GM^2/R)$ is the NS binding energy. Combining Equations (5) and (6) we finally get

$$\frac{E_{pol}}{E_T} \gtrsim \frac{0.0814}{(\Gamma/\gamma - 1)} \frac{E_{tor}}{E_G}. \quad (7)$$

[7] The factor $(\Gamma/\gamma - 1) \sim f_p/2 \simeq$ a few % in an NS core, where f_p is the charged particle fraction (Reisenegger & Goldreich 1992).

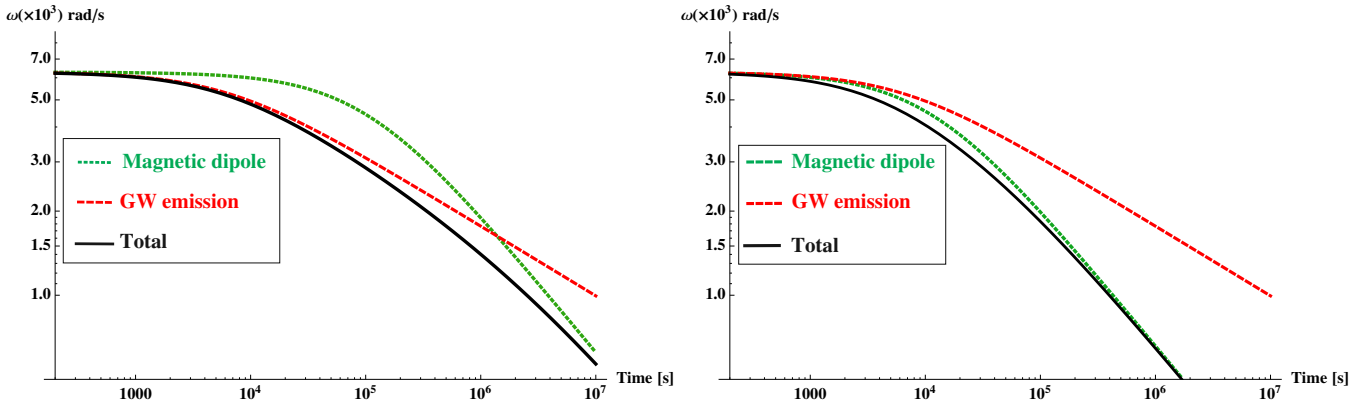

Figure 2. Spindown of a PMNS born with a spin period of 1 ms, in two representative cases. Left panel: initially the GW-induced torque dominates and a strong GW signal can be emitted. The dipole magnetic field is $B_{\rm dip} \simeq 10^{14}\,G$ and the interior toroidal field energy corresponds to $\epsilon_{\rm B} \simeq 10^{-3}$. As the spin frequency decreases the electromagnetic torque progressively kicks in, while the amplitude and frequency of the GW signal both decay faster than they would if only GW emission were effective. Right panel: the spindown is dominated from the beginning by the electromagnetic torque. Here $B_{\rm dip} \simeq 3 \times 10^{14}\,G$ and the same $\epsilon_{\rm B} \simeq 10^{-3}$. No strong GW signal is expected in this case, but a bright electromagnetic transient, e.g., a short GRB extended emission or plateau, could result.

Assuming $f_p \simeq 0.05$ (Reisenegger & Goldreich 1992) the coefficient $\Gamma/\gamma - 1 \simeq 0.02$, hence the stability condition reads

$$\left(\frac{E_T}{10^{50}\ {\rm erg}}\right) \lesssim 3\left(\frac{B_{\rm dip}}{10^{14}\ G}\right)\left(\frac{\Gamma/\gamma - 1}{0.02}\right)\left(\frac{R_*}{15\ {\rm km}}\right)\left(\frac{M_*}{2.36\ M_\odot}\right). \quad (8)$$

This suggests that, at the end of the amplification process, a massive magnetar can be formed with a *stable* mixed field dominated by the toroidal component. The latter can, in principle, tap the energy $\gtrsim 10^{50}$ erg that was originally in differential rotation, e.g., for the magnetic configuration of Figure 1. The strength of the exterior dipole will be determined by the total energy in the poloidal field *and* by the size of the closed-field-line region.

Finally, by adopting the scalings of Equation (3), we can write the stability condition (8) as

$$\frac{E_T}{E_{\rm pol}} \lesssim 545\left(\frac{B_{\rm dip}}{10^{14}\ G}\right)^{-1}\left(\frac{M}{2.36\ M_\odot}\right)\left(\frac{R_*}{15\ {\rm km}}\right)^{-2}\left(\frac{\Gamma/\gamma - 1}{0.02}\right). \quad (9)$$

2.3. Spindown of the Newly Formed NS

A rotating ellipsoid with the symmetry axis tilted with respect to the spin axis by an angle χ has a GW-induced spindown luminosity (Cutler & Jones 2001, and references therein)

$$\dot{E}_{\rm GW} = -\frac{2}{5}\frac{G(I\epsilon_{\rm B})^2}{c^5}\omega_s^6 \sin^2\chi\,(1 + 15\sin^2\chi), \quad (10)$$

where ν_s is the spin frequency and $\omega_s = 2\pi\nu_s$.

Once the prolate ellipsoid has become an orthogonal rotator, the GW-induced spindown is maximized and the resulting spindown formula becomes

$$\dot{E}_{\rm GW} = -\frac{32}{5}\frac{G(I\epsilon_{\rm B})^2}{c^5}\omega_s^6, \quad (11)$$

which we will use throughout this work.

When the additional torque due to the dipole magnetic field is included, the total spin down of the PMNS becomes

$$\dot{\omega}_s = -\frac{B_{\rm dip}^2 R^6}{6Ic^3}\omega_s^3 - \frac{32}{5}\frac{GI\epsilon_{\rm B}^2}{c^5}\omega_s^5, \quad (12)$$

where $B_{\rm dip}$ is the dipole field at the NS pole[8] and R the PMNS radius.

In Figure 2, we plot the solution of Equation (12) in two representative cases, showing the critical role of the ratio between the interior toroidal field and the exterior dipole in setting the intensity and duration of the spindown-induced GW signal. When GW emission initially dominates the spindown, it will do so only for a limited time after which magnetic dipole takes over. If magnetic dipole braking dominates at birth, on the other hand, it will do so even at later times due to its weaker dependence on ω. In this case, the PMNS spin energy is released electromagnetically and could produce observables, e.g., plateaus in SGRBs (Rowlinson et al. 2013; also see Dall'Osso et al. 2011 for long GRBs).

In this paper, we will only be concerned with the GW signal, thus we aim at determining the conditions under which the GW torque dominates the PMNS spindown. However, we will be interested in tracking the spindown for as long as possible since the population of potential sources, *stable* and supramassive PMNSs, will display distinctive features in the evolution of their signals. The GW signal emitted by a stable PMNS will be characterized by steadily decreasing frequency and amplitude, with dipole braking significantly accelerating the evolution at late times. On the other hand, the collapse of the supramassive object will truncate the signal, thus leaving a very specific signature.

2.4. Orthogonalization Timescale

Given the near alignment implied by the initial conditions, significant GW emission will ensue only after the tilt angle χ has become large. During this very early phase, the PMNS is, however, subject to magnetic dipole braking, with a spindown time $\tau_{\rm em,i} = \omega_i/(2\dot{\omega}_i) \simeq 1$ day $B_{\rm dip,14}^2 P_{i,\rm ms}^2$. A necessary condition for the PMNS to be able to radiate its huge spin energy reservoir via GWs is that the growth time of the tilt angle, τ_χ, be shorter than $\tau_{\rm em,i}$. In the opposite case, a bright electromagnetic transient of duration $\sim\tau_{\rm em,i}$ would carry away much of the initial spin energy, leaving much less energy available for GW emission once χ has grown significantly.

Dall'Osso et al. (2009) derived the expression $\tau_\chi \sim 13 {\rm E}_{\rm T,50} P_{\rm ms}^2 T_{10}^{-6}$ s, where the strong temperature dependence is

[8] The magnetic dipole moment is $\mu_{\rm d} = B_{\rm dip}R^3/2$.

due to bulk viscosity being the most important dissipation mechanism. Using this expression, they calculated the time for the tilt angle to grow to, e.g., $\pi/3$ rad, explicitly accounting for the fact that the very efficient modified-URCA reactions cause the NS temperature to change significantly during the process. They concluded that, for the region of parameter space where GW spindown wins over magnetic dipole braking, orthogonalization is always achieved in a time significantly shorter than $\tau_{\rm em.i}$.

3. STABLE VERSUS UNSTABLE MAGNETARS: DIFFERENT EOS AND TIME OF COLLAPSE

Whether a merger forms, a stable or a supramassive PMNS will depend on the mass of the binary components and on the maximum mass ($M_{\rm max}$) allowed by the NS EOS. A stable PMNS can be formed in the merger of a relatively low-mass BNS (Giacomazzo & Perna 2013), for a sufficiently stiff EOS that allows a maximum NS mass $M_{\rm max} \gtrsim 2.3\,M_\odot$. For a given EOS, fast rotation[9] provides additional support against collapse, increasing the mass limit by up to ∼20% when break-up speed is approached (Lyford et al. 2003). Supramassive PMNSs could thus be formed in a wider range of conditions and may well represent a large fraction of the whole population, especially when considering the softer EOS among those consistent with the observational constraint $M_{\rm max} > 2.1\,M_\odot$.

NS masses generally refer to the gravitational mass, M_g, the corresponding rest-mass being approximately[10] (Timmes et al. 1996)

$$M_r = M_g + 0.075\,M_g^2\,. \quad (13)$$

For a given EOS the equilibrium mass of a NS is a function of the central density, $\hat{M}_g(\rho_c)$, and the maximum mass $M_{g,\rm max}$ indicates the peak in this function. Models with $M_g > M_{g,\rm max}$ are unstable and immediately collapse to BHs when rotation is negligible.

When rotation is included one can formally write the equilibrium mass as a function of the spin period P, or of the rotation rate Ω, as (Lasky et al. 2014; Ravi & Lasky 2014)

$$\hat{M}_g(P;\,\rho_c) = \hat{M}_g(\rho_c) + \Delta M(P;\,\rho_c) = \hat{M}_g(\rho_c)(1+\alpha\,P^{-\beta}), \quad (14)$$

where both coefficients α and β depend on the star's EOS.[11] The maximum mass, $M_{g,\rm max}(P_{\rm min})$, now depends explicitly on the maximum allowed rotation rate, i.e., the mass-shedding limit $\Omega_{\rm max}$ or the corresponding minimum period $P_{\rm min}$. The latter is given, to an accuracy of a few percent, by (Stergioulas 2003 and references therein)

$$\Omega_{\rm max} = \mathcal{C}(\chi_s)\sqrt{GM_{g,\rm max}/R_{\rm max}^3}, \quad (15)$$

where $M_{g,\rm max}$ and $R_{\rm max}$ are the mass and radius of the maximum mass nonrotating model, $\chi_s = 2GM_{g,\rm max}/(c^2 R_{\rm max})$ its compactness, and the function $\mathcal{C}(\chi_s) = 0.468 + 0.378\chi_s$. Comparing with, e.g., the numerical results of Lasky et al. (2014) for three selected EOS, gives indeed a very good agreement.

The EOS GM1 used by Lasky et al. (2014) has $M_{g,\rm max} = 2.37\,M_\odot$ and $R_{\rm max} = 12$ km, corresponding to $\chi_s \simeq 0.586$ and $\Omega_{\rm max} \simeq 9.3\times10^3$ rad s^{-1} ($P_{\rm min} \simeq 0.67$ ms). For this EOS, $\alpha = 1.58\times10^{-10}$ and $\beta = 2.84$ (Lasky et al. 2014), giving $M_{g,\rm max}(P_{\rm min}) \simeq 2.77\,M_\odot$. For comparison, Giacomazzo & Perna (2013) adopted a polytropic EOS with $n = 4/7$ and $K = 30,000$ that well approximates the behavior at high density of the EOS by Shen et al. 1998 (see Oechslin et al. 2007). This polytropic EOS has a maximum mass $M_{g,\rm max} \sim 2.43\,M_\odot$ (and radius ∼12 km) for a nonrotating NS, while the maximally rotating model[12] has a maximum $M_{g,\rm max}(P_{\rm min}) \sim 2.95\,M_\odot$ (see Giacomazzo & Perna 2013 for more details). Finally, a relatively softer EOS that is widely used is the APR (Akmal et al. 1998) with $M_{g,\rm max} = 2.2\,M_\odot$, $R_{\rm max} = 10$ km, $\alpha = 3.03\times10^{-11}$ and $\beta = 2.95$ (Lasky et al. 2014). With these figures, we get $P_{\rm min} \simeq 0.51$ ms and $M_{g,\rm max}(P_{\rm min}) \simeq 2.54\,M_\odot$.

Based on the measured masses of nine BNSs, the mass distribution of NSs in binaries was found to be peaked at $\langle M_g\rangle \simeq (1.32\pm0.11)\,M_\odot$ (Kiziltan et al. 2013) which corresponds to $\langle M_r\rangle \simeq (1.45\pm0.13)\,M_\odot$, with the errors indicating a 68% probability interval. A "typical" equal-mass binary would have $M_r = (2.91\pm0.18)\,M_\odot$, or $M_g = (2.45\pm0.13)\,M_\odot$, close to the maximum for the $n = 4/7$ polytrope described above, but uncomfortably large, e.g., the APR EOS. Such numbers suggest that, for the $n = 4/7$ EOS (or, possibly, the GM1), a large majority of BNS mergers would produce either a supramassive or a stable PMNS, with the latter potentially representing a sizeable fraction. A BH would be the most likely result for softer EOS, possibly with a small fraction of supramassive PMNSs rotating close to break-up.

To further clarify this point, we plot in Figure 3 the measured NS masses in nine BNSs (Kiziltan et al. 2013, their Table 1) along with lines indicating $M_{g,\rm max}$ for the EOS GM1 and the $n = 4/7$ polytrope. These lines assume that the total rest-mass is conserved in the merger: any loss of rest-mass due to, e.g., mass ejection or the formation of a disk/torus around the remnant, would shift them upward in the plot. For three systems only the total gravitational mass is well determined, hence we plot them separately showing the 68% probability range for the total mass in the right panel of Figure 3.

4. SOURCE DETECTION

Three main factors determine the rate at which GW signals of massive magnetars formed in BNS mergers can be revealed with advanced detectors: (1) the total rate of BNS mergers, $\dot{\mathcal{N}}$, and the fraction of such events that will form a massive PMNS, call it $p_{\rm ns}$; (2) the intrinsic signal strength as a function of the physical properties of the sources; (3) the detector's properties.

4.1. Signal-to-noise Ratio

The maximum strain received from an ideally oriented[13] NS spinning at frequency ν_s and at a distance D is

$$h(f) = \frac{4\pi^2 G I \epsilon_{\rm B}}{c^4 {\rm D}}\,f^2, \quad (16)$$

where $f = 2\nu_s$ is the frequency of the GW signal.

As the detector collects the signal, the NS spins down and both frequency and strain decrease. The signal-to-noise ratio

[9] We only consider uniform rotation here.

[10] This accounts for the NS binding energy, including leading-order relativistic corrections as well as finite entropy effects.

[11] This is true for relativistic models, while in Newtonian models $\beta = 2$ and only α depends on the stellar structure.

[12] The formulae for rotating models give $\Omega_{\rm max} \simeq 9.52\times10^3$ rad s^{-1} ($P_{\rm min} \simeq 0.66$ ms).

[13] Ideal orientation to the detector's arms and optimal angle between spin and line of sight.

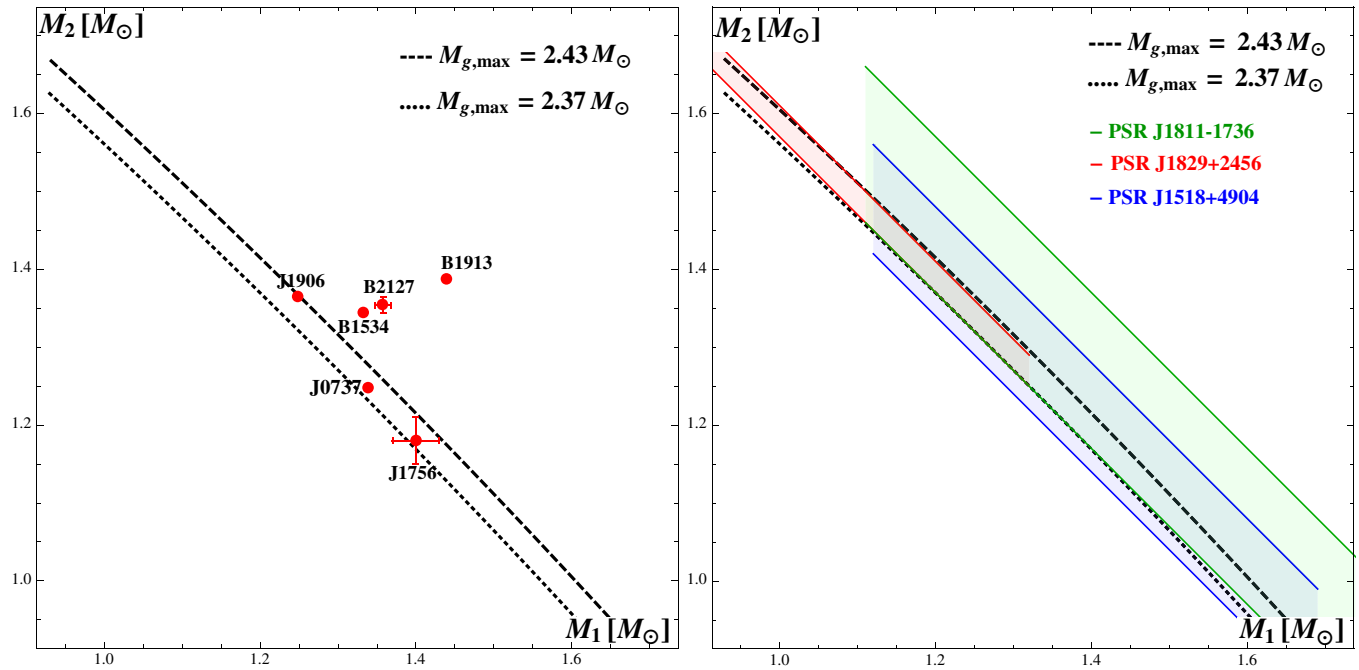

Figure 3. Left panel: measured gravitational masses for NSs in BNSs (Kiziltan et al. 2013). Points below the diagonal lines indicate systems that will potentially form a stable PMNS, i.e. $M_g < M_{g,\max}$, for two different EOS: (a) a polytrope with $n = 4/7$ and $K = 30{,}000$, that well approximates the nuclear EOS by Shen et al. 1998 (dashed line); (b) GM1 from Lasky et al. 2014 (dotted line). The two lines are obtained assuming the conservation of rest-mass in the merger and an approximate $M_r - M_g$ relation (see the text). Mass-loss shifts the lines upward. For example, the two lines are separated by a rest-mass difference of $\simeq 0.04\,M_\odot$. Right panel: for three BNSs, individual masses are loosely constrained and only the total gravitational mass is well determined. The 1σ error ranges (Kiziltan et al. 2013) are plotted: PSR J1829+2456 falls between the two lines. Conclusions are uncertain for the remaining systems.

(S/N) for an ideal matched-filter search is thus defined as

$$\mathrm{S/N} = 2\left[\int_{f_i}^{f_f} df\,\frac{|\tilde{h}(f)|^2}{S_h(f)}\right]^{1/2}, \tag{17}$$

where $S_h(f)$ is the detector's (one-sided) noise spectral density and $\tilde{h}(f)$ is the Fourier transform of $h[f(t)]$. The latter will depend on the frequency spindown (see Sathyaprakash & Schutz 2009), hence on both $B_{\rm dip}$ and $\epsilon_{\rm B}$, in general (see Dall'Osso et al. 2009). It is useful for our purposes to write it in the limit where df/ft is only due to GW emission

$$\left(\frac{S}{N}\right)_{\rm GW} \simeq 10\left(\frac{D}{33.5\ \mathrm{Mpc}}\right)^{-1}\left(\frac{R}{15\ \mathrm{km}}\right)\left(\frac{M}{2.36\,M_\odot}\right)^{1/2} \times\left[\left(\frac{f_f}{\mathrm{kHz}}\right)^{-2}-\left(\frac{f_i}{\mathrm{kHz}}\right)^{-2}\right]^{1/2}. \tag{18}$$

The choice of the low end of the frequency range, f_f, can be very important for the value of S/N, while f_i has a marginal role as long as it is not too close to f_f. This will be a crucial point in the next section, where we aim at assessing the effective detectability of our sources.

4.2. The Detector's "Range" $\mathcal{R}$

The intensity of a received GW signal also depends on the source's direction and on the orientation of its spin axis with respect to the line of sight. At a fixed detection threshold, favorably oriented sources are detectable out to much larger distances than badly oriented, yet identical, ones. A proper average of these orientation-dependent horizons, which accounts for the probability of different sources making different angles with respect to the detector's arms and having different angles between their spin axes and the lines of sight, is the detector's "range," $\mathcal{R}$ (Finn & Chernoff 1993). This allows us to write the total rate of detectable events simply as[14]

$$\dot{N}_{\rm det} = \frac{4}{3}\pi\dot{\mathcal{N}}\,p_{\rm ns}\mathcal{R}^3\,. \tag{19}$$

Note that *not all* detected sources will actually be within $\mathcal{R}$: some will be farther away, but with a particularly favorable orientation while others, that are well within $\mathcal{R}$, will go undetected being unfavorably oriented.[15]

If we define the optimal horizon $D_{\rm opt}$ as the maximum distance at which an optimally oriented source can be detected with an ideal matched-filter search made using one single interferometer, then the range is simply obtained as $\mathcal{R} = D_{\rm opt}/2.26$ (see section 4.3 in Finn & Chernoff 1993).

For a single-detector search, we set, for simplicity, the detection threshold at S/N = 8 (Abadie et al. 2010). We do not need to determine it more accurately at this stage, in view of the significant improvement in sensitivity that the operation of a network of detectors will guarantee over the single-detector case (Schutz 2011). For this reason, the estimates that follow may well be regarded as conservative ones.

The maximum distance at which S/N is above threshold, $D_{\rm opt}$, can only be obtained as a function of source parameters. In particular, given the dependence of S/N on f_f (Equation (18)),

[14] We just added the factor $p_{\rm ns}$ to the formula given by Finn & Chernoff (1993).

[15] The fraction of detected sources that will be beyond a given distance can also be estimated (Finn & Chernoff 1993).

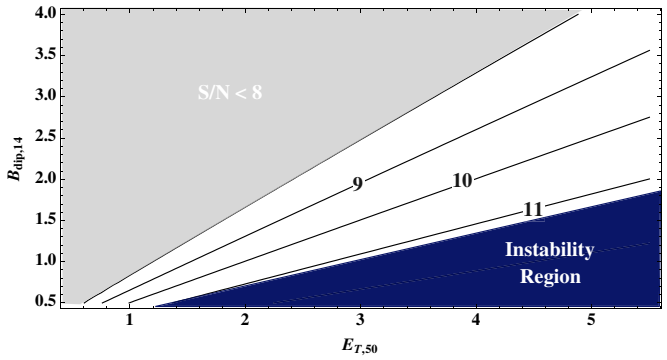

Figure 4. Contours of the optimal S/N in the B_d vs. E_T plane, for a single detector search and an ideally oriented source at a distance of 75 Mpc. We define this, somewhat arbitrarily, as the maximum distance at which S/N is above the threshold in a sufficiently large region of the parameter space (about half). Following Abadie et al. (2010), the threshold for detectability is set at S/N = 8. No NS can be found in the instability region defined by inequality (8).

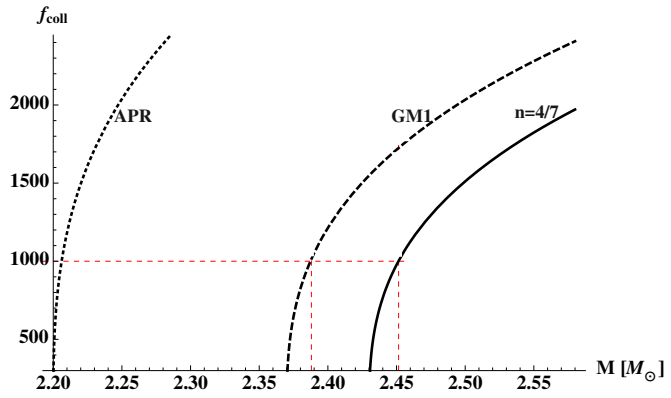

Figure 5. Signal frequency at which a supramassive PMNS collapses, $f_{coll} = 2\nu_{s,coll}$ vs. the initial mass, for the three selected EOS discussed in Section 3. The red dashed lines indicate the initial mass at which $f_{coll} = 1$ kHz (spin period of 2 ms), with only lower initial masses collapsing at lower frequencies, implying a narrow range of allowed masses $\Delta M \simeq 0.02\,M_\odot$ for the $n = 4/7$ and GM1 EOS. For the APR EOS the allowed range is $\Delta M < 0.01\,M_\odot$.

we will consider stable and supramassive NSs separately. Indeed, while f_f for the former is determined by spindown causing a decrease of the signal amplitude (Figure 2), for the latter, it is determined by the collapse of the NS which, in general, occurs much earlier (see below).

4.2.1. Stable PMNS

If a stable PMNS is formed in the merger, a strong GW signal starts within a few tens of minutes, once the angle between the rotation axis and the symmetry axis of the toroidal field has grown sufficiently. The initial frequency is $f_i = 2\nu_{s,i}$ and GWs should dominate the spindown, initially, in order for the signal to be detectable at all. As the PMNS spin frequency decreases, the magnetic dipole torque becomes relatively more important (see Equation (12)), the signal amplitude and frequency decay progressively faster than they would under pure GW emission, and GW emission eventually fades away once the spin down is dominated by the magnetic dipole. This determines the lower end of the frequency interval, f_f.

We have calculated S/N according to Equation (17) including self-consistently both torques in the expression for the spindown. Since S/N depends on two parameters (B_{dip}, E_B), the distance up to which it remains above threshold is not unequivocally determined. We choose as our horizon a distance at which S/N $\geqslant$ 8 for approximately half of the parameter space of interest, which turns out to be $D_{opt} \simeq 75$ Mpc for a PMNS with $M = 2.36\,M_\odot$, $R = 15$ km and $\nu_{s,i} = 1$ kHz (see Giacomazzo & Perna 2013), translating to $\mathcal{R} \simeq 33.5$ Mpc. The S/N contours in the $B\int_d$ versus $\int E_B$ plane for this specific configuration are shown in Figure 4, where the range of the two magnetic field components was chosen appropriately for our case.

4.2.2. Supramassive PMNS

The collapse of a supramassive PMNS sets the frequency $= f_{coll}$. It occurs when the star's mass, M_{ns}, equals the maximum mass at a given spin period, $M_{g,max}(P_{min})$. By inverting the definition of $\hat{M}_g(P;\rho_c)$ of Section 3, we can write (Lasky et al. 2014)

$$f_{coll} = 2\left(\frac{M_{ns} - M_{g,max}}{\alpha M_{g,max}}\right)^{1/\beta}, \qquad (20)$$

the solution of which is plotted in Figure 5, as a function of M_{ns}, for the three selected EOS discussed in Section 3. In general, the frequency at collapse decreases with the mass and becomes lower than 1 kHz only if M_{ns} lies in an extremely narrow range just above $M_{g,max}$. A much lower S/N than for stable PMNSs is thus expected, which implies a smaller horizon and a much smaller number of events. One must restrict attention to the smallest masses in order to get the strongest signals, visible to the largest distances. However, this reduces drastically the number of possible targets.

For an approximately Gaussian distribution of remnant masses peaked at $2.45\,M_\odot$ and with $\sigma_M = 0.13\,M_\odot$ (see Section 3), only ~5% and 6% of them would lie between $M_{g,max}$ and $(M_{g,max} + 0.02)\,M_\odot$, for the GM1 and the $n = 4/7$ EOS, respectively. This fraction becomes quickly negligible for softer EOS, while for stiffer EOS most mergers would produce stable PMNSs given that $M_{g,max}$ is above the Gaussian peak. For illustration, we have considered a $2.45\,M_\odot$ remnant with $R = 15$ km and initially spinning at break up, $\nu_{s,i} \simeq 1500$ Hz for the $n = 4/7$ polytrope. According to Equation (20) it will collapse when $f_{coll} \simeq 1$ kHz, or the spin period ≃2 ms. We derived the optimal horizon for this relatively favorable case as was done in the previous section. The result is shown in Figure 6 with $D_{opt} = 35$ Mpc, corresponding to $\mathcal{R} \simeq 16$ Mpc. This considerably smaller horizon compared to the stable PMNSs causes a factor 10 reduction in the sampling volume. Together with the small fraction of objects that fall in this favorable mass range, it implies that a number ~100–200 times smaller of such events can be detected compared to the stable PMNSs.

4.3. The Expected Event Rate

In light of the above findings, the number of PMNSs that can be revealed with the forthcoming generation of GW detectors will be dominated by stable PMNSs, and will strongly depend on the NS EOS. The discussion of Section 3, summarized in Figure 3, suggests that a sizeable fraction, $p_{ns} \sim 0.2$–0.5, of the whole population of BNS mergers could result in a stable or marginally supramassive PMNS for the GM1 or the $n = 4/7$ polytropic EOS. This fraction grows to ~ unity for harder EOS's, in particular, those with $M_{g,max} \geqslant 2.5\,M_\odot$. For relatively softer EOS's like, e.g., the APR; on the other hand, the maximum mass quickly becomes too low and essentially all mergers would immediately produce a BH. The detection of a ~ kHz frequency GW signal with hour-long spindown following a BNS merger, as

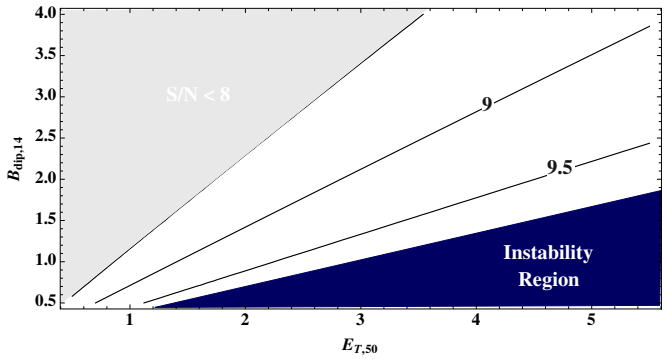

Figure 6. Contours of the optimal S/N in the B_d vs. E_T plane, for a single detector search, and an ideally oriented *supramassive* PMNS at $D_{opt} = 35$ Mpc. We chose $M_g = 2.45\,M_\odot$, $R = 15$ km, and an $n = 4/7$ ($K = 3000$) polytropic EOS, for which the breakup frequency is 1500 Hz, and the collapse frequency $f_{coll} \simeq 1$ kHz. With the initial spin frequency taken to be at breakup, we have $f_i = 3$ kHz and $= f_{coll} \simeq 1$ kHz. We define D_{opt}, somewhat arbitrarily, as the maximum distance at which the S/N is above threshold in a sufficiently large region of the relevant parameter space. No NS can be found in the instability region defined by Equation (8).

discussed here, would thus provide a very interesting constraint on the EOS of NS matter. This would be especially valuable when combined with an independent determination of the total population of BNS, which could provide a direct measure of the fraction p_{ns}.

Since $N_{det} \propto \dot{\mathcal{N}}$ (see Equation (19)), we can express the rate of detection of PMNS signals relative to the rate of detection of BNS mergers with advanced detectors as

$$\frac{\dot{N}_{det}}{\dot{\mathcal{N}}} \sim p_{ns} \left(\frac{\mathcal{R}_{PMNS}}{\mathcal{R}_{BNS}}\right)^3 \sim 0.003, \qquad (21)$$

where $\mathcal{R}_{BNS} \sim 170$ Mpc (Abadie et al. 2010) and we assumed $p_{ns} \sim 0.3$ (thus excluding EOSs softer than the GM1). In this case, the small fraction mostly reflects the difference in the sampling volume for the two different types of signals.

"Realistic" estimates of the detection rates of BNS mergers with advanced detectors range from 40 to 400 events per year (Abadie et al. 2010), and were derived phenomenologically based on a statistical study of the population of known BNS in the Galaxy (Kalogera et al. 2004). By adopting these numbers, we conclude that stable PMNSs may be detectable at a rate of $\dot{N}_{set} \sim (0.1 - 1)$ yr^{-1} with Advanced detectors, for the GM1 or the $n = 4/7$ polytropic EOS. For stiffer EOS, with $M_{g,max} \gtrsim 2.5\,M_\odot$, nearly all mergers would produce a PMNS, thus the detection rate could be higher by a factor of $\approx$3. For softer EOS, on the other hand, these figures drop significantly following the drop in the coefficient p_{ns}.

We finally note that third generation detectors, such as the Einstein Telescope, will have a higher sensitivity by up to a factor of $\sim$10 (Punturo et al 2010). This will increase the detector's range, $\mathcal{R}$ by the same factor, making stable PMNSs detectable up to $\mathcal{R} \gtrsim 300$ Mpc, and even supramassive ones up to $\mathcal{R} \gtrsim 150$ Mpc. The detection rate will thus increase by a very large factor, $\sim 10^3$, which is extremely important, in particular, for supramassive PMNSs. Indeed, with advanced detectors these objects will also become interesting sources, with a likely rate of detection of a few events per year.

5. SUMMARY AND DISCUSSION

The GW signatures of a newly born NS are very sensitive to the EOS. Intense GW emission is expected under the presence of a strong toroidal magnetic field, as a result of the star's prolate ellipsoidal shape. In such a configuration, viscous dissipation drives the magnetic symmetry axis orthogonal to the spin axis, hence maximizing the strength of the emitted GW radiation.

GWs from highly magnetized NSs newly born in core collapse supernovae have been studied in a number of works. Here, motivated by recent numerical simulations of binary NS mergers which show magnetic field amplification, we have studied the conditions under which strong GW emission is expected in the post-merger phase, if this is characterized by the presence of a short-lived, or stable, highly magnetized NS. To this aim, we have extended the set of equilibrium states for a twisted torus magnetic configuration to include solutions that, for a given external dipolar field, carry a larger magnetic energy reservoir. We have then computed the magnetic ellipticity for such configurations, hence the strength of the GW signal, once the system has orthogonalized.

We find that the strength of the signal, and hence its detectability, is mainly dependent on the NS EOS. The dependence is twofold. First, whether the merger of two NSs leads to a supramassive NS (which eventually collapses to a BH) or to a stable NS, is highly dependent on the NS EOS. For a given distribution of remnant masses, stiffer EOSs yield a higher fraction of stable NSs. Second, the GW signal itself, and, in particular, the two distinct and robust spectral features that characterize the post-merger emission, are very sensitive to the NS EOS (e.g., Takami et al. 2014). For an intermediate EOS, such as the $n = 4/7$ polytrope, or the GM1 used by Lasky et al. (2014), we estimate that we expect GW emission from PMNSs in about 0.3% of all GW detections from BNS mergers. Correspondingly, we expect a detection rate of about 0.1–1 events per year with advanced detectors; this rate would increase by a factor of $\sim 10^3$ with third generation detectors, such as the Einstein Telescope, which will have a higher S/N by up to a factor of 10. These detectors would be able to observe even the weaker emission from the unstable PMNSs, albeit with lower rates.

GWs from highly magnetized PMNSs produced in mergers would be especially interesting if detected in connection with a short GRB. In fact, while there is plenty of circumstantial evidence that these events are produced by a merger, whether the final product is a stable (or unstable) NS, or a promptly formed BH is still a subject of investigation. Extended emission, occasionally in the form a plateau, has been seen in about half of *Swift* SGRBs. In some cases, this emission ends abruptly (possibly indicating the collapse of a hypermassive NS to a BH), while in some other cases it declines with a power law, possibly indicating the presence of a stable NS (Rowlinson et al. 2013). Detection of GWs from the PMNS would allow us to discern its identity, and hence shed light on the nature of the binary progenitors of SGRBs. In addition, contemporary detections of an SGRB and GWs would further constrain the NS EOS (e.g., Giacomazzo et al. 2013).

For this work, S.D. was supported by the SFB/Transregio 7, funded by the Deutsche Forschungsgemeinschaft (DFG). B.G. acknowledges support from MIUR FIR Grant No. RBFR13QJYF, and R.P. from NSF grant No. AST 1009396 and NASA grant No. NNX12AO67G.

APPENDIX

A.1. The Twisted-torus Configuration

In spherical coordinates, the interior poloidal field is

$$B_{\rm pol}(\hat{r},\theta) = B_0[\eta_{\rm pol}\nabla\hat{\alpha}(\hat{r},\theta)\times\nabla\hat{\phi} + \eta_{\rm T}\hat{\beta}(\hat{r},\theta)\nabla\hat{\phi}], \quad \text{(A1)}$$

where $\hat{r} = r/R_{\rm ns}$ is the dimensionless radial coordinate and $\nabla\hat{\phi} = \hat{\phi}/(\hat{r}\sin\theta)$, with $\hat{\phi}$ as the unit vector in the ϕ-direction. B_0 is a normalization (in Gauss), $\hat{\alpha}$ the (adimensional) flux function, *i.e.,* the poloidal magnetic flux threading a polar cap of radius $\tilde{\omega} = R_*\hat{r}\sin\theta$, $\eta_{\rm pol}$ and $\eta_{\rm T}$ are dimensionless constants measuring the relative strength of the two field components and the "current function" $\hat{\beta} \equiv \hat{\beta}(\hat{\alpha})$, as required by axysimmetry. Since no currents exist in the exterior, this implies that electrical currents can only flow on poloidal field lines that close *inside* the NS, hence the bounding region for $B_{\rm T}$. In particular, $\hat{\beta} = (\hat{\alpha}-1)^n$ is usually assumed, with $n > 1$ to ensure regularity of the supporting currents at the boundary of the toroidal field region. Finally, the exterior dipole field is matched at the NS surface to the interior field by taking the flux function $\hat{\alpha}(\hat{r},\theta) = f(\hat{r})\sin^2\theta$.

The function f is determined[16] by first imposing the magnetic force and current density to remain finite everywhere inside the NS. For a trial form $f(\hat{r}) \propto \hat{r}^p$ this implies either $p = 2$ or $p > 3$, suggesting a polynomial solution for f. Smoothly matching the interior and exterior fields requires continuity of the magnetic field at the NS surface, and that no surface currents exist. To satisfy this at least three terms in the polynomial are needed; therefore, the "simplest" solution is $f(\hat{r}) = c_2\hat{r}^2 + c_4\hat{r}^4 + c_5\hat{r}^5$. The coefficients are determined by normalization of $f(\hat{r})$, thus fixing the field shape. Different choices for the polynomial terms are, however, possible, which affect the shape and size of the closed-field-line region. For the purpose of this work, we have chosen the configuration represented in Figure 1, which corresponds to $f(\hat{r}) = (435/8)\hat{r}^2 - (1221/4)\hat{r}^4 + 400\hat{r}^5 - (1185/8)\hat{r}^6$ and $\hat{\beta} = (\hat{\alpha}-1)^2$.

A.2. Magnetic Ellipticity

The two components of the inertia tensor I_{zz} and I_{xx} are obtained through the magnetically induced density perturbation by (Mastrano et al. 2011)

$$I_{jk} = R_*^5\int d\mathrm{V}[\rho(\hat{r}) + \delta\rho(\hat{r},\theta)]\left(\hat{r}^2\delta_{jk} - \hat{x}_{jk}^2\right). \quad \text{(A2)}$$

With these definitions, the total ellipticity is eventually expressed as

$$\epsilon_{\rm B} = \frac{\pi R_*^5}{I_0}\int d\theta d\hat{r}\delta\rho(\hat{r},\theta)\hat{r}^4\sin\theta(1-3\cos^2\theta), \quad \text{(A3)}$$

hence the relation between the magnetic field structure and the induced ellipticity of the NS is obtained directly from $\delta\rho(\hat{r},\theta)$. To calculate the latter, we follow the steps described by Mastrano et al. (2011), who write the equation of hydrostatic equilibrium to first order in the magnetic perturbation in the Cowling approximation,

$$-\frac{B_0^2}{\hat{r}^2\sin^2\theta}\left(\eta_{\rm pol}^2\nabla\hat{\alpha}\hat{\Delta}\hat{\alpha} + \eta_{\rm T}^2\hat{\beta}\nabla\hat{\beta}\right) = \nabla\delta p + \delta\rho\nabla\Phi\,. \quad \text{(A4)}$$

[16] A full derivation is given by Akgün et al. (2013).

Here δp is the magnetically induced pressure perturbation, Φ the unperturbed gravitational potential, and the Grad–Shafranov operator is $\hat{\Delta} = \partial_{\hat{r}}^2 + (\sin\theta/\hat{r}^2)\partial_\theta[(\sin\theta)^{-1}\partial_\theta]$. The θ-component of Equation (A3) relates the magnetic term to δp alone. Feeding the latter in the $\hat{r}$-component gives the density perturbation inside the NS as a function of $\hat{\alpha}, \hat{r}, \theta$ and the parameters (B_0, $\eta_{\rm T}$, $\eta_{\rm pol}$). The poloidal and toroidal field contribute with opposite signs to $\delta\rho(\hat{r},\theta)$, hence the ellipticity due to the poloidal field is positive according to our definition, while the toroidal field produces a negative $\epsilon_{\rm B}$. Solving Equation (A3) for $\delta\rho(\hat{r},\theta)$ with our chosen $\hat{\alpha}(\hat{r},\theta)$, we plug it into Equation (A2) to eventually obtain the *total* magnetic ellipticity of the NS reported in Equation (1).

REFERENCES

Abadie, J., Abbott, B. P., Abbott, R., et al. 2010, CQGra, 27, 173001
Akgün, T., Reisenegger, A., Mastrano, A., & Marchant, P. 2013, MNRAS, 433, 2445
Akmal, A., Pandharipande, V. R., & Ravenhall, D. G. 1998, PhRvC, 58, 1804
Andersson, N., Baker, J., Belczynski, K., et al. 2013, CQGra, 30, 193002
Antoniadis, J., Freire, P. C. C., Wex, N., et al. 2013, Sci, 340, 448
Baiotti, L., Giacomazzo, B., & Rezzolla, L. 2008, PhRvD, 78, 084033
Bauswein, A., Baumgarte, T. W., & Janka, H.-T. 2013, PhRvL, 111, 131101
Berger, E. 2014, ARA&A, 52, 43
Braithwaite, J. 2009, MNRAS, 397, 763
Braithwaite, J., & Nordlund, Å. 2006, A&A, 450, 1077
Bucciantini, N., Quataert, E., Arons, J., Metzger, B. D., & Thompson, T. A. 2008, MNRAS, 383, L25
Bucciantini, N., Thompson, T. A., Arons, J., Quataert, E., & Del Zanna, L. 2006, MNRAS, 368, 1717
Cutler, C. 2002, PhRvD, 66, 084025
Cutler, C., & Jones, D. I. 2001, PhRvD, 63, 024002
Dall'Osso, S., Granot, J., & Piran, T. 2012, MNRAS, 422, 2878
Dall'Osso, S., Shore, S. N., & Stella, L. 2009, MNRAS, 398, 1869
Dall'Osso, S., & Stella, L. 2007, Ap&SS, 308, 119
Dall'Osso, S., Stratta, G., Guetta, D., et al. 2011, A&A, 526, A121
Demorest, P. B., Pennucci, T., Ransom, S. M., Roberts, M. S. E., & Hessels, J. W. T. 2010, Nature, 467, 1081
Duncan, R. C., & Thompson, C. 1992, ApJL, 392, L9
Faber, J. A., & Rasio, F. A. 2012, LRR, 15, 8
Falcke, H., & Rezzolla, L. 2014, A&A, 562, 137
Finn, L. S., & Chernoff, D. F. 1993, PhRvD, 47, 2198
Giacomazzo, B., & Perna, R. 2013, ApJL, 771, L26
Giacomazzo, B., Perna, R., Rezzolla, L., Troja, E., & Lazzati, D. 2013, ApJL, 762, L18
Giacomazzo, B., Rezzolla, L., & Baiotti, L. 2011, PhRvD, 83, 044014
Giacomazzo, B., Zrake, J., Duffel, P., MacFaydin, A., & Perna, R. 2014, arXiv:1410.0013
Hotokezaka, K., Kyutoku, K., Okawa, H., Shibata, M., & Kiuchi, K. 2011, PhRvD, 83, 124008
Kalogera, V., Kim, C., Lorimer, D. R., et al. 2004, ApJL, 601, L179
Kiziltan, B., Kottas, A., De Yoreo, M., & Thorsett, S. E. 2013, ApJ, 778, 66
Lasky, P. D., Haskell, B., Ravi, V., Howell, E. J., & Coward, D. M. 2014, PhRvD, 89, 047302
Lorimer, D. R., Bailes, M., McLaughlin, M. A., Narkevic, D. J., & Crawford, F. 2007, Sci, 318, 777
Lyford, N. D., Baumgarte, T. W., & Shapiro, S. L. 2003, ApJ, 583, 410
Mastrano, A., & Melatos, A. 2012, MNRAS, 421, 760
Mastrano, A., Melatos, A., Reisenegger, A., & Akgün, T. 2011, MNRAS, 417, 2288
Metzger, B. D., Giannios, D., Thompson, T. A., Bucciantini, N., & Quataert, E. 2011, MNRAS, 413, 2031
Metzger, B. D., Quataert, E., & Thompson, T. A. 2008, MNRAS, 385, 1455
Oechslin, R., Janka, H.-T., & Marek, A. 2007, A&A, 467, 395
Perna, R., & Pons, J. A. 2011, ApJL, 727, L51
Pons, J. A., & Perna, R. 2011, ApJ, 741, 123
Punturo, M., Abernathy, M., Acernese, F., et al. 2010, CQGra, 27, 194002
Ravi, V., & Lasky, P. D. 2014, MNRAS, 441, 2433
Rea, N., Esposito, P., Turolla, R., et al. 2010, Sci, 330, 944

Rea, N., Israel, G. L., Esposito, P., et al. 2012, ApJ, 754, 27
Rea, N., Israel, G. L., Pons, J. A., et al. 2013, ApJ, 770, 65
Reisenegger, A. 2009, A&A, 499, 557
Reisenegger, A., & Goldreich, P. 1992, ApJ, 395, 240
Rezzolla, L., Baiotti, L., Giacomazzo, B., Link, D., & Font, J. A. 2010, CQGra, 27, 114105
Rowlinson, A., O'Brien, P. T., Metzger, B. D., Tanvir, N. R., & Levan, A. J. 2013, MNRAS, 430, 1061
Sathyaprakash, B. S., & Schutz, B. F. 2009, LRR, 12, 2
Schutz, B. F. 2011, CQGra, 28, 125023
Shen, H., Toki, H., Oyamatsu, K., & Sumiyoshi, K. 1998, NuPhA, 637, 435
Stella, L., Dall'Osso, S., Israel, G. L., & Vecchio, A. 2005, ApJL, 634, L165
Stergioulas, N. 2003, LRR, 6, 3
Takami, K., Rezzolla, L., & Baiotti, L. 2014, PhRvL, 113, 091104
Timmes, F. X., Woosley, S. E., & Weaver, T. A. 1996, ApJ, 457, 834
Thornton, D., Stappers, B., Bailes, M., et al. 2013, Sci, 341, 53
Viganò, D., Rea, N., Pons, J. A., et al. 2013, MNRAS, 434, 123
Zhang, B., & Mészáros, P. 2001, ApJL, 552, L35
Zrake, J., & MacFadyen, A. I. 2013, ApJL, 769, L29